

A NUMERICAL AND EXPERIMENTAL INVESTIGATION INTO THE CRACKING OF FIBRE REINFORCED CEMENTITIOUS MATERIALS

IULIA C. MIHAI*

* Cardiff University

School of Engineering, Queen's Buildings, The Parade, Cardiff, CF24 3AA, UK

e-mail: mihaic1@cardiff.ac.uk

Key words: Fiber Reinforced Concrete, Cracking, Digital Image Correlation, Micromechanics, Constitutive Modelling

Abstract: Adding short fibres to cementitious materials improves their resistance to cracking. The fibres introduce crack-bridging mechanisms that reduce cracking, improve post-fracture mechanical behaviour and increase toughness. The accurate and efficient prediction of cracking in quasi-brittle materials with numerical models is a long-standing challenge.

A constitutive model for fibre reinforced cementitious composites based on continuum micromechanics solutions is presented. The model assumes a two-phase elastic composite, derived from an Eshelby solution and the Mori-Tanaka scheme [1], which comprises a matrix phase representing the mortar and spherical inclusions representing the coarse aggregate particles. Additionally, circular microcracks with various orientations are distributed within the matrix phase. An exterior point Eshelby based criterion is employed to model crack-initiation in the matrix-inclusion interface. Microcrack surfaces are assumed to be rough and able to regain contact under both normal and shear displacements. Once cracks start to develop, the crack-bridging action of fibres is simulated using a local constitutive equation that accounts for the debonding and pull-out of fibres with different orientations [2]. It is shown that the combination of the rough microcrack and fibre-bridging sub-models allows microcracking behaviour deriving from both tensile and compressive loads to be modelled in a unified manner.

Numerical results obtained with the proposed micromechanical constitutive model are compared with experimental data. Good correlation between numerical and experimental responses demonstrates the potential of the model to capture key characteristics of the mechanical behaviour of fibre reinforced cementitious composites. Furthermore, the performance of the model when implemented in a finite element code is assessed. Finite element predictions are compared against experimental results from a series of flexural tests on fibre reinforced concrete beams in which the development and evolution of cracks was tracked on the surface of the specimens using Digital Image Correlation (DIC) equipment.

1 INTRODUCTION

Randomly distributed short fibres have been added to cementitious materials since ancient times but their use has expanded greatly over past half century [3]. They endow brittle cement-bound materials with enhanced

tensile strength, and their inclusion in cementitious matrices can delay the onset of macro-cracking and enhance both ductility and durability [3].

The behaviour of cementitious composites reinforced with randomly distributed and

oriented discontinuous fibres is largely governed by fibre pull-out. When a crack is initiated and opens, the fibres crossing the crack plane start to debond and are subsequently pulled out. In this process, they apply closure tractions to the crack faces and stabilise the crack growth. Through these crack-bridging mechanisms, the fibres continue to transfer stresses between the two crack faces until their complete pull-out.

The paper presents an experimental and numerical study into the cracking of fibre reinforced concrete.

The progression of surface cracks in reinforced concrete (RC) beams which contained different amounts of steel fibres was studied in a series of flexural tests monitored with a DIC system (Section 2).

Section 3 presents a constitutive model that builds on a series of micromechanics based models for plain concrete [4-6] which are in turn extended to simulate the mechanical behaviour of fibre reinforced concrete [2].

Results from single-point and finite element simulations employing the proposed constitutive model for FRC and compared against experimental data, are presented in Section 4.

2 EXPERIMENTAL STUDY OF FRC/RC BEAMS SUBJECTED TO FLEXURE

Concrete beams (120 x 150 x 2000 mm) containing conventional reinforcement and varying amounts of randomly distributed short fibres were tested using the experimental setup shown in Figure 2 in which all dimensions are in mm. Varying volume fractions of Dramix steel fibres ($L_f = 60\text{mm}$ and $d_f = 0.71\text{mm}$) were used in manufacturing the specimens as presented in Table 1. All beams were provided with $1\phi 10\text{mm}$ rebar flexural reinforcement and $\phi 6\text{mm}$ shear links 50mm c/c. After curing for 14 days the beams were subjected to 4-point bending under mid-point displacement control. A DIC system was used to monitor the progression of surface cracks throughout the tests.

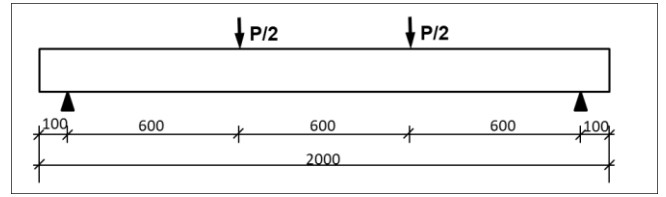


Figure 1. Experimental setup

Table 1. Experimental test specimens

Batch code	V_f (by volume)
Control	0%
SFRC1	1%
SFRC2	2%

The load – mid-point displacement responses for the different specimens are presented in Figure 2. The results show an increase in load carrying capacity and in ductility with the addition of fibres. The crack patterns obtained with the DIC system are shown in Figure 3 for control and SFRC2 beams respectively, for a mid-point displacement of 15 mm. It can be observed that with the addition of fibres cracking becomes more distributed; SFRC2 beams present with a larger number of cracks and smaller crack spacing than the control beams.

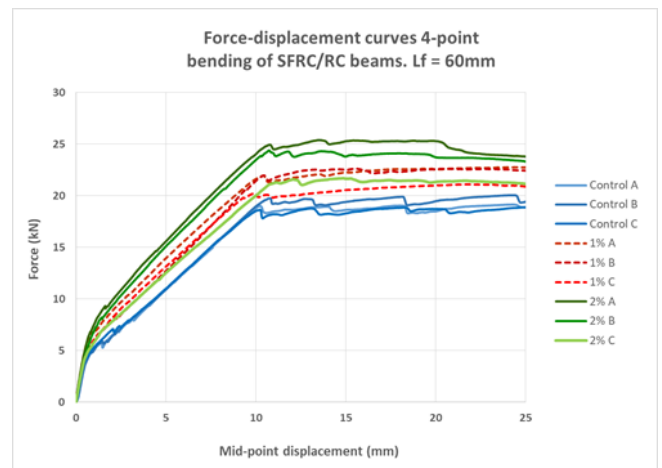


Figure 2. Experimental force-displacement response

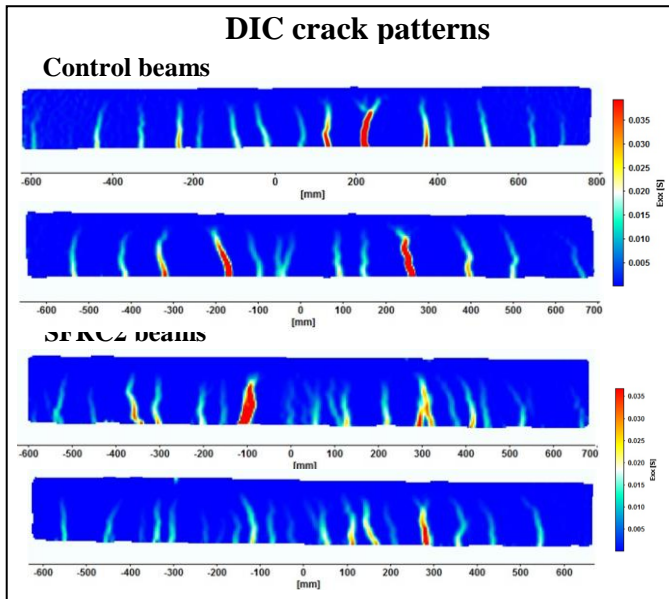


Figure 3. DIC crack patterns for control and SFRC2 specimens respectively

3 MICROMECHANICS BASED CONSTITUTIVE MODEL FOR FRC

3.1 Model concepts

A summary of the constitutive model for FRC with key equations is presented in this sections, but full details are available in Mihai & Jefferson [2]. The general concepts of the model are presented in Figure 4. The concrete matrix of the fibre reinforced material is modelled as a two-phase solid material that comprises series of penny-shaped microcracks which can have various orientations, defined by ψ and θ (Figure 4b). It is assumed that the effect of each series of cracks with the same orientation is equivalent to that of a thin band of material containing these cumulated microcracks (Figure 4c) and, as damage progresses, they can coalesce and form macro-cracks. The mid-plane of the thin band is referred to as a ‘crack-plane’. Moreover, in each direction, the corresponding crack-plane is crossed by randomly distributed and oriented short fibres. The model also assumes that cracks have rough surfaces that can regain contact.

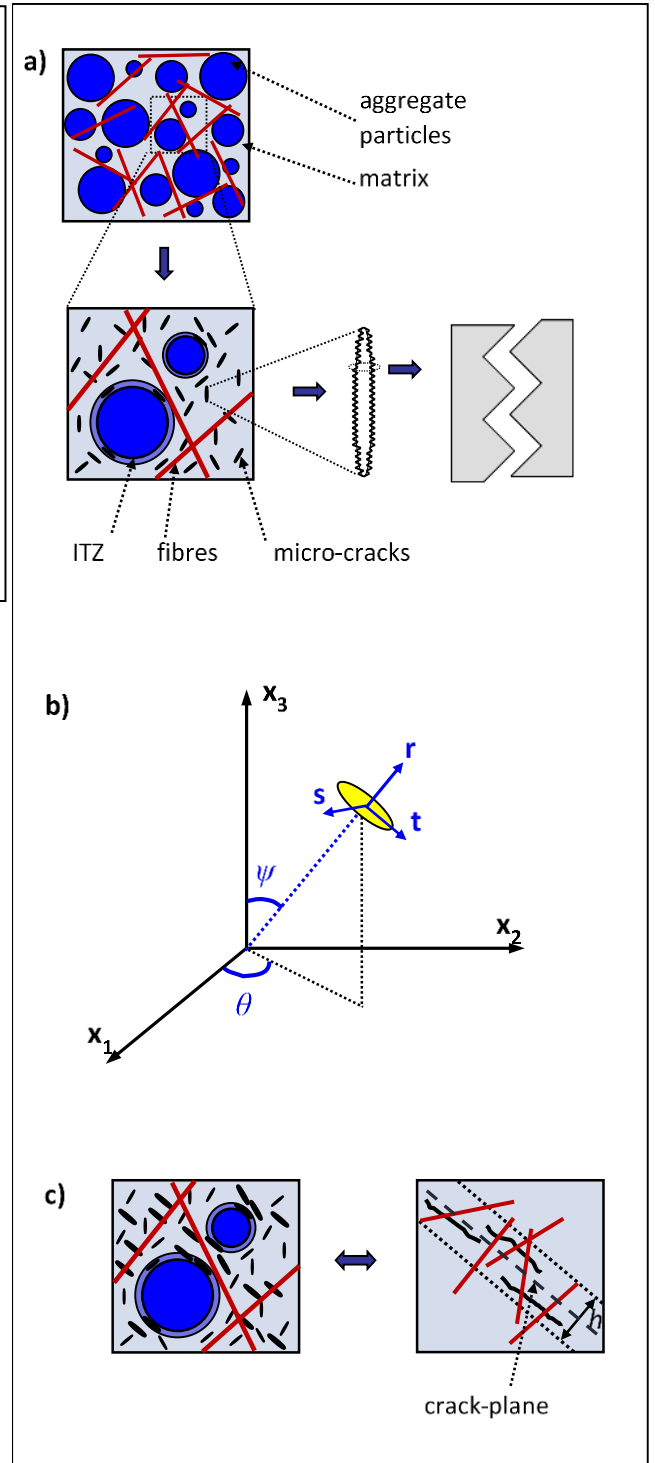


Figure 4. a) Model concepts. b) Local coordinate system. c) Schematic representation of the crack-plane

3.2 Two-phase composite

The elastic constitutive relationship for the two-phase composite is obtained by making use of the micromechanics Eshelby matrix-inclusion solution and the Mori-Tanaka homogenisation scheme [1] for a non-dilute

distribution of inclusions:

$$\bar{\boldsymbol{\sigma}} = \mathbf{D}_{m\Omega} : \bar{\boldsymbol{\varepsilon}} \quad (1)$$

where $\bar{\boldsymbol{\sigma}}$ and $\bar{\boldsymbol{\varepsilon}}$ are the average far-field stress and strain respectively. $\mathbf{D}_{m\Omega}$ is the elasticity tensor of the composite given by:

$$\mathbf{D}_{m\Omega} = (f_m \mathbf{D}_m + f_\Omega \mathbf{D}_\Omega \cdot \mathbf{T}_\Omega) \cdot (f_m \mathbf{I}^{4s} + f_\Omega \mathbf{T}_\Omega)^{-1} \quad (2)$$

in which \mathbf{D}_β represents the elasticity tensor and f_β the volume fraction of β -phase ($\beta = m$ or Ω), $f_m + f_\Omega = 1$. \mathbf{I}^{4s} is the fourth order identity tensor and:

$$\mathbf{T}_\Omega = \mathbf{I}^{4s} + \mathbf{S}_\Omega \cdot [(\mathbf{D}_\Omega - \mathbf{D}_m) \cdot \mathbf{S}_\Omega + \mathbf{D}_m]^{-1} \cdot (\mathbf{D}_m - \mathbf{D}_\Omega) \quad (3)$$

\mathbf{S}_Ω is the Eshelby tensor for spherical inclusions [1].

3.3 Directional microcracking

A solution based on the work of Budiansky & O'Connell [7] is employed to address microcracking by evaluating the added strain $\boldsymbol{\varepsilon}_a$ from series of penny-shaped microcracks of various orientations distributed according to a crack density function $f(\theta, \psi)$. The added strains resulting from the microcracks are superimposed on the composite such that the constitutive Equation 1 becomes:

$$\bar{\boldsymbol{\sigma}} = \mathbf{D}_{m\Omega} : (\bar{\boldsymbol{\varepsilon}} - \boldsymbol{\varepsilon}_a) \quad (4)$$

And the added strain are as follows [7]:

$$\boldsymbol{\varepsilon}_a = \left(\frac{1}{2\pi} \int_{-\pi/2}^{\pi/2} \int_0^{2\pi} \mathbf{N}_\varepsilon : \mathbf{C}_a : \mathbf{N} f(\theta, \psi) \sin(\psi) d\psi d\theta \right) : \bar{\boldsymbol{\sigma}} \quad (5)$$

in which \mathbf{C}_a is the local compliance tensor in the local coordinate system of a microcrack $(\mathbf{r}, \mathbf{s}, \mathbf{t})$ and \mathbf{N} the stress transformation tensor. The crack density parameter is related to a directional microcracking parameter ω ($0 \leq \omega \leq 1$) such that:

$$f(\theta, \psi) \mathbf{C}_a = \frac{\omega(\theta, \psi)}{1 - \omega(\theta, \psi)} \mathbf{C}_L = \mathbf{C}_\alpha(\theta, \psi) \quad (6)$$

where $\mathbf{C}_L = \frac{1}{E_m} \begin{bmatrix} 1 & 0 & 0 \\ 0 & \frac{4}{2-\nu_m} & 0 \\ 0 & 0 & \frac{4}{2-\nu_m} \end{bmatrix}$ is the local

elastic compliance tensor, with ν_m and E_m being Poisson's ratio and Young's modulus of the matrix phase respectively. Introducing

Equation 5 and Equation 6 into Equation 4 and rearranging gives:

$$\bar{\boldsymbol{\sigma}} = \left(\mathbf{I}^{4s} + \frac{\mathbf{D}_{m\Omega}}{2\pi} \int_{-\pi/2}^{\pi/2} \int_0^{2\pi} \mathbf{N}_\varepsilon : \mathbf{C}_\alpha(\theta, \psi) : \mathbf{N} \cdot \sin(\psi) d\psi d\theta \right)^{-1} \cdot \mathbf{D}_{m\Omega} : \bar{\boldsymbol{\varepsilon}} \quad (7)$$

3.4 Microcrack initiation criterion

The crack initiation criterion proposed by Mihai & Jefferson [6] is employed here; microcracking in each direction is assumed to initiate in a band of matrix material within the interfacial transition zone (ITZ), when the local principal stress in this band reaches the tensile strength of the interface (f_{ii}). The initial damage surface, F_s is given by:

$$F_s(\boldsymbol{\sigma}_L, f_{ii}) = \sigma_I(\boldsymbol{\sigma}_L) - f_{ii} = 0 \quad (8)$$

where $\boldsymbol{\sigma}_L$ is the local stress which is related to the average far-field stress as follows:

$$\boldsymbol{\sigma}_L(\psi, \theta) = \mathbf{N}(\psi, \theta) : \bar{\boldsymbol{\sigma}} \quad (9)$$

The local stresses in the thin band of matrix material in the ITZ are evaluated based on the exterior point Eshelby solution [8] which gives the expression of the total stress field outside an ellipsoidal inclusion embedded in an infinite elastic matrix [9]. The Mori-Tanaka homogenization scheme is applied in order to account for the interaction between inclusions and the total stress field in the matrix outside an inclusion is obtained as:

$$\boldsymbol{\sigma}_{m\Omega}(\mathbf{x}) = \mathbf{D}_m \cdot \left[\mathbf{I}^{4s} + \mathbf{S}_E(\mathbf{x}) \cdot \mathbf{B}_\Omega \right] \cdot \left[f_\Omega \mathbf{T}_\Omega + f_m \mathbf{I}^{4s} \right]^{-1} : (\bar{\boldsymbol{\varepsilon}} - \boldsymbol{\varepsilon}_a) \quad (10)$$

in which $\mathbf{B}_\Omega = -\left[\mathbf{S}_\Omega + (\mathbf{D}_\Omega - \mathbf{D}_m)^{-1} \cdot \mathbf{D}_m \right]^{-1}$.

$\mathbf{S}_E(\mathbf{x})$ is the exterior point Eshelby tensor for spherical inclusions, derived in a dimensionless form in Li et al. [10] and \mathbf{x} is the position vector relative to the centre of inclusion. A local microcracking function was subsequently derived from the local crack initiation criterion in Equation 8 and is given by:

$$F_{\zeta}(\boldsymbol{\varepsilon}_L, \zeta) = \varepsilon_{Lrr} \frac{1 + \alpha_L}{2} + \sqrt{\varepsilon_{Lrr}^2 \left(\frac{1 - \alpha_L}{2} \right)^2 + r_L^2 (\varepsilon_{Lrs}^2 + \varepsilon_{Lrt}^2)} - \zeta \quad (11)$$

in which $\alpha_L = \frac{\nu_m}{1 - \nu_m}$, $r_L = \frac{\nu_m - 1/2}{\nu_m - 1}$ and noting that the following loading/unloading conditions apply:

$$F_{\zeta} \leq 0; \quad \dot{\zeta} \geq 0; \quad F_{\zeta} \dot{\zeta} = 0 \quad (12)$$

3.5 Rough crack contact

A rough crack closure component is also implemented to simulate the recovery of stress on microcracks that regain contact. In each direction the local stress was written as a summation of the average stress on intact material and the recovered stress on debonded material that regains contact:

$$\mathbf{s}_{\alpha} = \mathbf{D}_L \left[(1 - \omega) \mathbf{I}^{2s} + \omega H_f(\boldsymbol{\varepsilon}_L) \boldsymbol{\Phi}(m_g, \boldsymbol{\varepsilon}_L) \right] : \boldsymbol{\varepsilon}_L \quad (13)$$

H_f is a reduction function that decreases from 1 to 0 as the potential for shear transfer reduces with increasing crack opening. This is given by $H_f(\boldsymbol{\varepsilon}_L) = e^{-c_I \frac{\varepsilon_{Lrr} - \varepsilon_{lm}}{\eta \cdot \varepsilon_0}}$ with $c_I = 3$, $\eta = h_f / u_0$, $\mathbf{D}_L = \mathbf{C}_L^{-1}$ and $\boldsymbol{\varepsilon}_L$ is the local strain tensor.

$\boldsymbol{\Phi}(m_g, \boldsymbol{\varepsilon}_L)$ is a contact matrix that depends upon the contact state (Figure 5) as follows:

$\boldsymbol{\Phi} = 0$, if crack surfaces are not in contact (open region)

$\boldsymbol{\Phi} = \boldsymbol{\Phi}_g$, if crack surfaces are in contact (interlock region)

$\boldsymbol{\Phi} = \mathbf{I}$, if are in fully closed region.

The expression of the contact matrix in the interlock region is:

$$\boldsymbol{\Phi}_g = \frac{1}{1 + m_g^2} \left(\left(\frac{\partial \varphi_{int}}{\partial \boldsymbol{\varepsilon}_L} \right) \left(\frac{\partial \varphi_{int}}{\partial \boldsymbol{\varepsilon}_L} \right)^T + \varphi_{int} \frac{\partial^2 \varphi_{int}}{\partial \boldsymbol{\varepsilon}_L^2} \right) \quad (14)$$

where:

$$\varphi_{int}(\boldsymbol{\varepsilon}_L, m_g) = m_g \varepsilon_{Lrr} - \sqrt{\varepsilon_{Lrs}^2 + \varepsilon_{Lrt}^2} \quad (15)$$

$$\varphi_{cl}(\boldsymbol{\varepsilon}_L, m_g) = \varepsilon_{Lrr} + m_g \sqrt{\varepsilon_{Lrs}^2 + \varepsilon_{Lrt}^2}$$

m_g is the slope of the interlock contact surface and, in a physical sense, it represents the slope of the asperity, thus being a measure of the crack surface roughness.

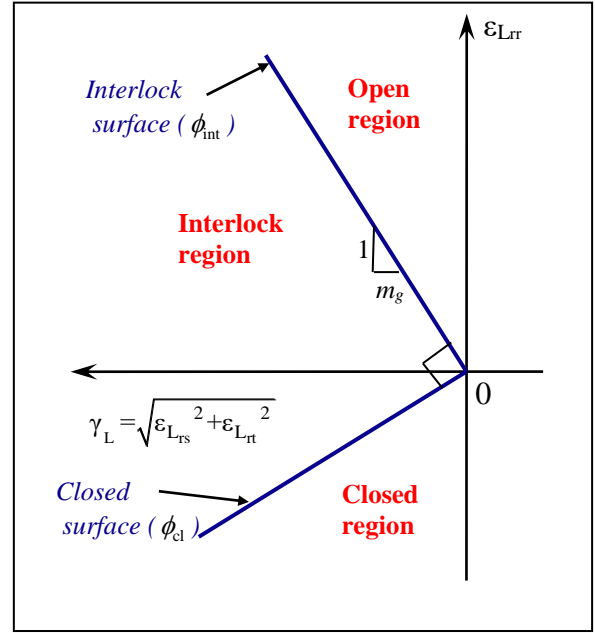


Figure 5. Contact model concepts

3.6 Crack bridging action of fibres

The influence of fibres is taken into account in the crack-plane stress – strain expression assuming that the fibre contribution develops after crack initiation. This is illustrated in Figure 6. In the case of fibre reinforced concrete Equation 13 becomes:

$$\mathbf{s}_{\alpha} = \left[(1 - \omega) \mathbf{D}_L + \omega (1 - \omega_f) \mathbf{D}_{fl} + \omega H_f(\boldsymbol{\varepsilon}_L) \mathbf{D}_L \cdot \boldsymbol{\Phi}(m_g, \boldsymbol{\varepsilon}_L) \right] : \boldsymbol{\varepsilon}_L \quad (16)$$

where ω_f is an effective fibre pull-out parameter that characterises the crack-bridging state of fibres and varies from 0, for a state before any fibre pull-out occurs, to 1, for a case in which all fibres are completely pulled out from the matrix. $\mathbf{D}_{Lf} = E_{df} \cdot \mathbf{I}^{2s}$ is a local elastic stiffness given by the interface bond of the fibres crossing the crack-plane, before the start of pull-out, assuming a linear debonding behaviour.

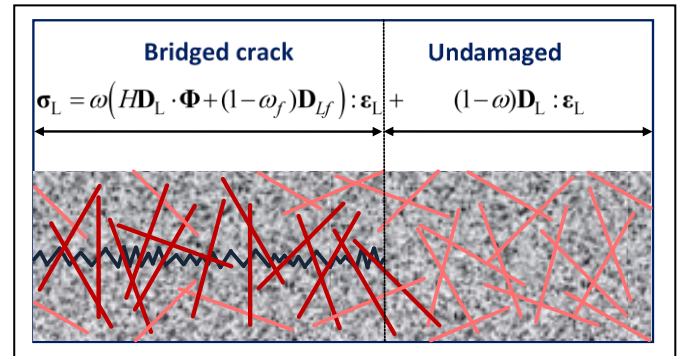


Figure 6. Crack-plane model with rough contact and fibre-bridging

The evolution of the effective fibre pull-out parameter ω_f is obtained from the following 1-D relation:

$$(1 - \omega_f)E_{df}\zeta_f = \sigma_{cb} \quad (17)$$

in which ζ_f is a resultant crack opening parameter that takes into account the normal and shear components of the crack-plane strain tensor and is governed by the effective fibre pull-out function given in Equation 18 and the loading/unloading conditions given in Equations 19:

$$F_{\zeta_f}(\boldsymbol{\varepsilon}_L, \zeta_f) = \frac{1}{2}\varepsilon_{Lrr} + \frac{1}{2}\sqrt{\varepsilon_{Lrr}^2 + 4(\varepsilon_{Lrs}^2 + \varepsilon_{Lrt}^2)} - \zeta_f \quad (18)$$

$$F_{\zeta_f} \leq 0; \quad \dot{\zeta}_f \geq 0; \quad F_{\zeta_f} \dot{\zeta}_f = 0 \quad (19)$$

σ_{cb} in Equation 17 is the crack bridging stress that is transferred between two opposing faces of a fully formed crack subjected to normal opening displacements, through the pull-out action of the fibres that cross the crack. The crack-bridging model of Lin & Li [11] is employed in which a crack-bridging stress – crack opening relationship was obtained by averaging the contributions from all fibres that cross the crack-plane during the debonding and the pull-out phases respectively:

$$\sigma_B(\delta) = \frac{4V_f}{\pi d_f^2} \int_{\varphi=0}^{\pi/2} \int_{z=0}^{(L_f/2)\cos\varphi} P(\delta)p(\varphi)p(z)dzd\varphi \quad (20)$$

in which V_f is the volume fraction of fibres, L_f and d_f are the length and diameter of the fibres respectively. $P(\delta)$ describes the debonding and pull-out force - displacement behaviour of a single fibre embedded in a concrete matrix, in a direction along the fibre axis. $p(\varphi)$ and $p(z)$ are probability density functions of the orientation angle φ and centriodal distance z respectively. The single fibre P - δ relation was derived assuming a linear slip-hardening interface constitutive relation between the fibre-matrix interface shear stress τ and the interface S :

$$\tau = \tau_0(1 + \beta S / d_f) \quad (21)$$

in which τ_0 is the frictional sliding shear stress at the tip of the debonding zone before any slip

takes place and β is a nondimensional hardening parameter. The two fibre-matrix interface parameters, τ_0 and β can be obtained from an experimental single fibre pull-out P - δ curve as detailed in[11].

Incorporating the rough crack contact and the crack-bridging effect of fibres, the final stress-strain model is:

$$\bar{\boldsymbol{\sigma}} = \left(\mathbf{I}^{4s} + \frac{\mathbf{D}_{m\Omega}}{2\pi} \int_{2\pi} \int_{\frac{\pi}{2}} \mathbf{N}_{\varepsilon} : \mathbf{C}_{\text{add}}(\theta, \psi) : \mathbf{N} \cdot \sin(\psi) d\psi d\theta \right)^{-1} \cdot \mathbf{D}_{m\Omega} : \bar{\boldsymbol{\varepsilon}} \quad (22)$$

where:

$$\mathbf{C}_{\text{add}} = \left[\mathbf{C}_L^{-1} \left[(1 - \omega) \mathbf{I}^{2s} + \omega \sum_i p_{ci} H_i \Phi_i \right] + \omega(1 - \omega_f) \mathbf{D}_n \right]^{-1} - \mathbf{C}_L \quad (23)$$

and in which the contact component was expanded and written as a weighted summation to account for the variability of the crack roughness. p_{ci} is the proportion, or the probability of the occurrence, of a certain type of asperity. The integration over a hemisphere in Eq. (21) is evaluated numerically by employing McLaren integration rule with 29 sample directions.

4 NUMERICAL RESULTS

4.1 Uniaxial tension

Numerical results for a uniaxial tension strain path obtained with the proposed micromechanical model and using a single set of realistic material properties (Table 2) are compared with experimental data of Li et al. [12] and presented in Figure 7. The numerical simulations compare well with experimental results; the model is able to predict the increase of strength and ductility of the composite with the in-crease of the fibre dosage.

Table 2. Material properties (Uniaxial tension test)

L_f (mm)	d_f (mm)	τ_0 (MPa)	β	E_m (GPa)	E_Ω (GPa)	f_i (MPa)
30	0.5	0.8	0.1	25	60	1.5

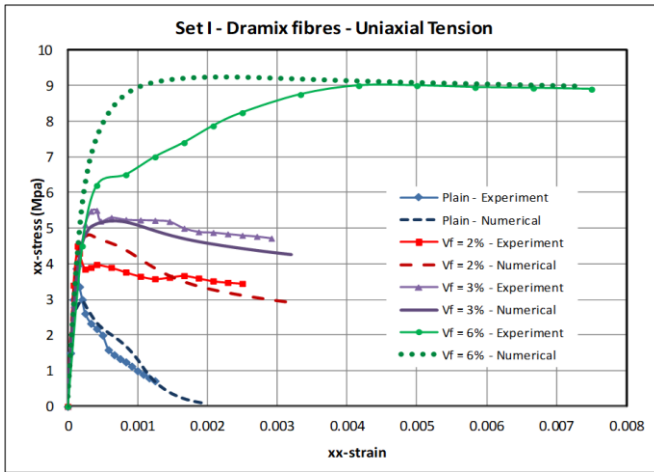


Figure 7. Numerical predictions of uniaxial tensile tests of Li et al. [12]

4.2 Uniaxial compression

Numerical results for a uniaxial compression strain path are next compared with experimental data of Cachim et al. [13] and presented in Figure 8. The material properties employed for the numerical simulations are presented in Table 3. Numerical predictions lie between experimental bounds and the model captures the slight increase in strength and an enhanced ductility of the FRC relative to plain concrete.

Table 3. Material properties (Uniaxial compression test)

L_f (mm)	d_f (mm)	τ_o (MPa)	β	E_m (GPa)	E_Ω (GPa)	f_{ii} (MPa)
30	0.5	1.0	0.1	17	44	1.5

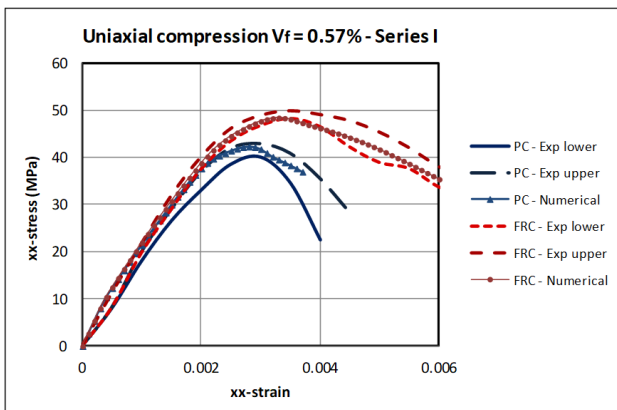


Figure 8. Numerical predictions of uniaxial compression tests of Cachim et al. [13]

4.2 FE simulations

The fibre model has been implemented in the commercial finite element software LUSAS and a numerical study based on the set of experimental tests from Section 2 is presented below.

Numerical analyses were carried out to simulate the experimental tests with the three types of specimens given in Table 1. In this work geometric properties from industrial data sheets for Dramix fibres were employed along with the set of material properties given in Table 4.

Table 4. Material properties (4 point bend test)

L_f (mm)	d_f (mm)	τ_o (MPa)	β	E_m (GPa)	E_Ω (GPa)	f_{ii} (MPa)
60	0.71	1.1	0.04	21	30	1.5

The finite element mesh with the boundary conditions used for the numerical analysis is presented in Figure 9. Finite element predictions of the load-deflection curves are compared with the experimental curves for the three sets of tests (Figure 10). The proposed model is able capture accurately the increase in capacity with increasing fibre content.

Plots of the major principal strains obtained from the finite element simulations showing the regions of localised damage are presented in Figures 11 & 12 for a mid-point displacement of 15mm. Plots of the experimental crack patterns obtained from the DIC monitoring are also presented in Figures 11 & 12.

It can be seen that with the addition of fibres cracking becomes more distributed and the model captures this characteristic well.

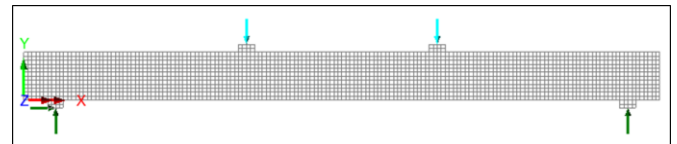


Figure 9. Finite element mesh

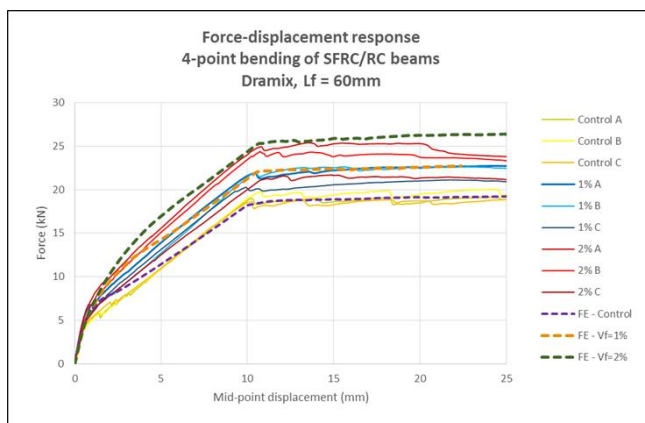


Figure 10. Force-displacement results

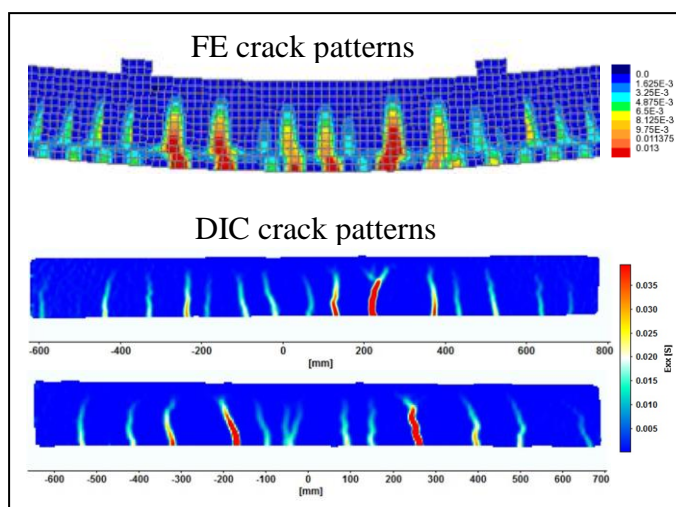


Figure 11. Numerical and experimental crack patterns. Control specimens

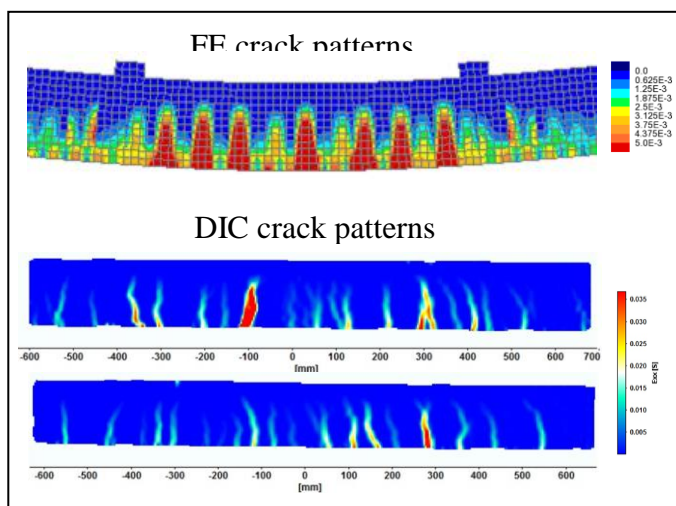


Figure 12. Numerical and experimental crack patterns. SFRC2 $V_f = 2\%$

5 CONCLUSIONS

An experimental study on cracking in FRC was presented and a constitutive model for FRC based on micromechanical solutions was

proposed. Good correlation between numerical results – obtained from both single-point and finite element simulation - and experimental data indicates that the proposed model captures correctly key characteristics of the overall macroscopic mechanical behaviour of fibre reinforced cement based composites, such as the increase of ductility and overall toughness of the fibre reinforced composite relative to the plain concrete matrix.

ACKNOWLEDGEMENTS

The author gratefully acknowledges the support of the finite element company LUSAS.

REFERENCES

- [1] Nemat-Nasser S, Hori M. 1999. Micromechanics: overall properties of heterogeneous materials. North-Holland
- [2] Mihai I.C, Jefferson A.D. 2017. A micromechanics based constitutive model for FRCCs. *Int J of Sol and Struct* 110, 152-169.
- [3] Naaman, A.E. 2008. Development and evolution of tensile strain-hardening FRC composites. *7th RILEM Intl Symp on FRC: Design and Applications - BEFIB 2008*, 1-28
- [4] Jefferson, A.D. & Bennett, T. 2007. Micro-mechanical damage and rough crack closure in cementitious composite materials. *Int J for Num and An Met in Geomech* 31: 133-146
- [5] Jefferson, A.D. & Bennett, T. 2010. A model for cementitious composite materials based on micro-mechanical solutions and damage-contact theory. *Comp and Struct* 88: 1361-1366
- [6] Mihai, I.C. & Jefferson, A.D. 2011. A numerical model for cementitious composite materials with an exterior point Eshelby microcrack initiation criterion. *Int J of Sol and Struct*, 48: 3312-3325
- [7] Budiansky B & O'Connell R.J. 1976. Elastic moduli of a cracked solid. *Int J of Sol & Struct*, 12: 81-97
- [8] Eshelby, J.D. 1959. The elastic field outside an ellipsoidal inclusion. *Proc of the Roy Soc A: Math Phys & Eng Sc*, 252(1271): 561-569
- [9] Ju JW & Sun L. 1999. A Novel Formulation for the Exterior-Point Eshelby's Tensor of an Ellipsoidal Inclusion. *J of Appl Mech, ASME*, 66: 570 – 574
- [10] Li S, Sauer RA & Wang G. 2007. The Eshelby Tensors in a Finite Spherical Domain – Part I. *J of Appl Mech, ASME*, 74: 770 – 783
- [11] Lin Z & Li VC. 1997. Crack bridging in FRCCs with slip-hardening interfaces. *J of the Mech & Phys of Sol* 45(5): 763-787
- [12] Li Z, Li F, Chang TYP & Mai YW. 1998. Uniaxial tensile behaviour of FRC. *ACI Mat J* 95(5): 564-574
- [13] Cachim P, Figueiras J & Pereira P. 2002. *Cem & Conc Res*, 24: 211-217